



Catalytic walls and micro-devices for generating hydrogen by low temperature steam reforming of ethanol

Albert Casanovas, Montserrat Domínguez, Cristian Ledesma, Eduardo López, Jordi Llorca*

Institut de Tècniques Energètiques, Universitat Politècnica de Catalunya, Av. Diagonal 647, Ed. ETSEIB, 08028 Barcelona, Spain

ARTICLE INFO

Article history:

Available online 21 October 2008

Keywords:

Hydrogen
Ethanol steam reforming
Monolith
Microreactor
Silicon micromonolith

ABSTRACT

Ethanol steam reforming ($S/C = 3$) was effectively performed at low temperature over catalytic wall reactors comprising a wide range of channel dimensions, ranging from conventional monoliths (channel width of 0.9 mm) to semicylindrical microchannels (0.35 mm radius) and to silicon micromonoliths (channel diameter of 3–4 μm). Co_3O_4 catalyst coatings were successfully prepared inside the channels from in situ thermal decomposition of two-dimensional layered cobalt hydroxide salts and showed a remarkable high homogeneity and mechanical stability. The Si-micromonolithic reactor proved extremely promising for hydrogen production for micro-fuel cell operation. Specific H_2 production rates exceeding 50 L_N of H_2 per mL of liquid and cm^3 of reactor were measured for ca. 42% ethanol conversion and residence times in the order of milliseconds.

© 2008 Elsevier B.V. All rights reserved.

1. Introduction

Motivated by the possibility of using hydrogen as an energy carrier and the rapid implementation of fuel cells, hydrogen production technologies are currently being investigated and developed thoroughly. In this context, the low temperature reforming of alcohols offers a nice solution for supplying hydrogen to portable fuel cells while avoiding safety and storage issues related to gaseous or liquid hydrogen. The use of alcohols for steam reforming is attractive due to their high volumetric energy density, low cost, safety, and easy transportation. Considerable work has been carried out on catalytic steam reforming of methanol and ethanol for hydrogen production using conventional packed bed reactors [1–4], but the use of micro-structured catalytic wall reactors is relatively new. In addition to compactness and light weight, the advantages of catalytic walls and microreactors include rapid mass and heat transport due to large surface area to volume ratios, low pressure drop and no reactor blocking, good structural and thermal stability, and precise control of process conditions with higher product yields. Micro-structured reactors also provide built-in safety because large volumes are avoided. Numerous micro-devices for on-site production of hydrogen from methanol steam reforming at 533–723 K have been reported [5], but although ethanol steam reforming is gaining interest rapidly

because ethanol is a renewable fuel easily produced from biomass (a bioethanol-to- H_2 system has the advantage of being CO_2 neutral), the higher temperatures required for C–C bond breaking has prevented extensive work in this field [6–8]. Herein, we report and compare the steam reforming of ethanol (Eq. (1)) at 673–773 K for hydrogen generation in small-scale portable devices over conventional monoliths (channel width ~ 0.9 mm), stainless-steel microreactors (channel diameter ~ 0.7 mm), and silicon micro-structured monoliths (channel diameter ~ 3 –4 μm) coated with thin layers of cobalt catalyst. Cobalt-based catalysts are known to exhibit good performance for the generation of hydrogen from steam reforming of ethanol at low temperature [9–21].



Decreasing the channel dimensions and pitch distance from conventional monoliths to microreactors and silicon micromonoliths results in a spectacular increase of inner surface area with respect to reactor volume, from about 10^3 to 10^5 $\text{m}^2 \text{m}^{-3}$ (Fig. 1), which means a much higher efficiency for hydrogen production in addition to the possibility of miniaturization for portable applications.

2. Experimental methods

2.1. Preparation of catalytic walls and micro-devices

Three different catalytic walls and micro-devices were used: (i) 400 and 900 cpsi (cells per square inch) cordierite monolith

* Corresponding author. Tel.: +34 93 401 17 08; fax: +34 93 401 71 49.
E-mail address: jordi.llorca@upc.edu (J. Llorca).

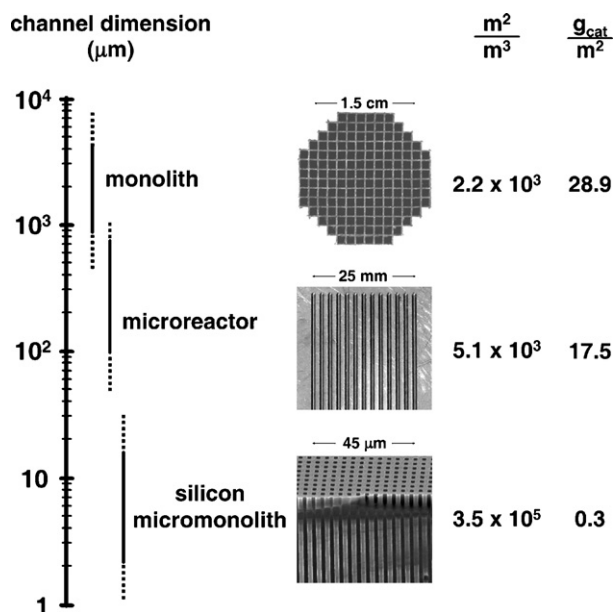


Fig. 1. Optical and scanning electron microscopy images of the catalytic substrates under study in the present work. Typical dimensions of the channels of each system, specific geometric surfaces, and catalyst loadings are included for comparison purposes.

cylinders with a diameter of ca. 2 cm and a length between 2 and 7 cm; (ii) a stainless-steel microreactor with thirteen 78 mm long, 700 μm wide, and 350 μm depth semicylindrical microchannels; and (iii) silicon micromonoliths with a diameter of about 7 mm containing ca. 1.5×10^6 microchannels with a diameter of 3.3 μm and a length of 210 μm. Details of the microreactor assembly and silicon micromonolith manufacture has been explained in detail in [7] and [8], respectively. Cobalt oxide was deposited in situ on the channel walls by thermal decomposition of hydrotalcite-like cobalt hydroxide prepared from the reaction of urea in cobalt(II) nitrate. First, a minimum amount of water or dimethylketone was added to a mixture of cobalt(II) nitrate and urea, with a Co:urea molar ratio between 1:1 and 1:4. Then, channels were completely filled with the solution (in some cases ZnO was added as a binder). A pressure gradient of 75 kPa was required in order to fill the channels of the silicon micromonoliths. The devices were then heated at 338 K under continuous rotation (60 rpm) along their channel direction for 4 h and a casting mixture was formed over the channels, which was subsequently heated at 383 K under rotation for 12 h. Finally, samples were calcined at 673 K for 4 h under air and reduced at 723 K for 1 h in 10% H₂/N₂.

2.2. Characterization techniques

The microstructure and morphology of catalytic walls were studied with a Hitachi H-2300 scanning electron microscope operating at 15 kV. Samples were sputtered with gold for ensuring good electron conductivity. Temperature-programmed reduction (TPR) was carried out with a Micromeritics AutoChem II 2920 instrument using a H₂/Ar mixture (5% H₂) at 10 K min⁻¹ and a TCD detector. Thermogravimetric analysis (TGA) was accomplished with a Q500 TA apparatus. Samples were heated up to 373 K (10 K min⁻¹), maintained at this temperature for 1 h, and then heated up to 723 K (5 K min⁻¹). Infrared spectra were collected using a Shimadzu FTIR 8400S spectrometer (resolution 2 cm⁻¹). X-ray diffraction profiles were collected with a Siemens D-500 instrument equipped with a Cu target and a graphite monochromator. Mechanical stability was evaluated by exposure to high

frequency ultrasounds (40 kHz) and by direct exposure to mechanical vibration (20–50 Hz and 2–10 G). G levels were controlled directly on the vibration test board with a Brüel & Kjaer 4370 accelerometer.

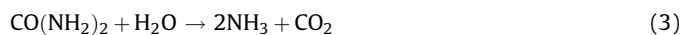
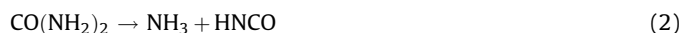
2.3. Catalytic studies

Catalytic tests were carried out at atmospheric pressure. Conventional monoliths and silicon micromonoliths were placed in a tubular, stainless-steel reactor. All three systems were disposed inside a temperature-controlled oven to operate at the selected temperature level. To perform tests under practical conditions, catalytic studies were conducted with a mixture of ethanol and water (*S/C* = 3) provided directly by a syringe pump (Genie Plus, Kent Scientific) at a rate between 8×10^{-4} and 1×10^{-1} mL min⁻¹. Liquid feed was evaporated in an external unit and conducted through thermostated pipes to the reactor inlet. In some experiments, the reactant mixture was diluted with N₂, from (C₂H₅OH + H₂O):N₂ = 1:0.05 to 1:2 on a molar basis. Contact times ranged from 2×10^{-3} to 2.5 s. Gaseous products were analyzed by online gas chromatography (Agilent 3000A MicroGC) using MS 5Å, PlotU and Stabilwax columns. Prior to catalytic tests, samples were prereduced in 10% H₂/N₂.

3. Results and discussion

3.1. Coating catalytic walls and microstructures

The conventional and easiest way for depositing catalyst coatings over catalytic walls, the washcoating method, proved to be inadequate for depositing thin, homogeneous catalyst layers of cobalt oxide on the walls of the microstructures used in this work. For that reason, we developed a new method based on the in situ thermal decomposition of hydrotalcite-like cobalt hydroxide precursors prepared from the reaction of urea in cobalt(II) nitrate, as detailed in Section 2.1. The decomposition of urea provided hydroxide groups (Eqs. (2)–(4)), which lead to the formation of two-dimensional layer hydroxide salts (LHS) with intercalated nitrate ions, Co(OH)_{2-x}(NO₃)_x·nH₂O [22]. LHS derive their structure from brucite and comprise a stacking of hydroxyl deficient positively charged layers having the composition [M(OH)_{2-x}]^{x+}. The structure incorporates anions in the interlayer region to restore charge neutrality. The thermal decomposition of LHS yielded well-dispersed and well-adhered cobalt oxide particles over the channels.



The synthesis procedure was followed by combining thermogravimetric analysis (TGA) with infrared spectroscopy (FTIR), and the final cobalt oxide product was characterized by X-ray diffraction (XRD), temperature-programmed reduction (TPR) and electron microscopy (SEM) in addition to FTIR. Fig. 2 corresponds to the TGA profile recorded over the solid mixture obtained after thermal treatment at 338 K for 4 h. Two steps were recognized. The weight loss recorded for the first step was gradual and likely due to water loss, whereas at ca. 450 K a single decomposition step occurred resulting in a weight loss of about 65%. This behavior does not correspond to the decomposition patterns of cobalt ureate or nitrate, which show four steps before the formation of cobalt oxide at a higher temperature [23]. Contrarily, single step weight loss is well documented in Co LHS with hydroxide and nitrate ions [24].

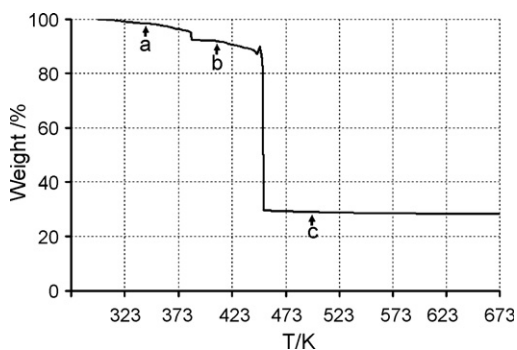


Fig. 2. Thermogravimetric analysis (air) of the cobalt nitrate–urea mixture after heating at 338 K. Labels (a–c) correspond to the infrared spectra of Fig. 3.

Fig. 3 shows the infrared spectra of this sample recorded after heating at 343, 413, and 513 K, which correspond to the three stages in the TGA profile. The infrared spectrum recorded for the sample heated at 343 K (Fig. 3a) showed broad bands at ca. 3000–3600 cm^{-1} , which are characteristic for the stretching mode of symmetric and antisymmetric hydrogen bonded OH groups. There was an absorption at 2190 cm^{-1} due to the isocyanate ion (NCO^-), which is one of the products of urea decomposition (Eq. (2)), and therefore can be expected to be included in the interlayer region during synthesis. Also, the band at 1627 cm^{-1} likely originated from intercalation of water in the van der Waal's gap between the hydroxide layers. The vibrations due to nitrate were observed in the intermediate wavenumber region. The appearance of four absorptions at 993 cm^{-1} (ν_2), 1340 cm^{-1} (ν_4), 1395 cm^{-1} (ν_3), and 1495 cm^{-1} (ν_1) indicated the incorporation of NO_3^- in C_{2v} symmetry. In LHS compounds the Co^{2+} ion occupies octahedral sites. The coordinative unsaturation of the metal ion in the 2D layers is satisfied by the nitrate anions, which are grafted directly to the metal ion. Accordingly, the large splitting, 155 cm^{-1} , between the ν_1 and ν_4 vibrational modes of the nitrate ion in the IR spectrum and the prominence and shifting of the ν_2 mode (from 1050 cm^{-1} in ionic systems to 993 cm^{-1}) revealed that one of the oxygen atoms of the nitrate group was bonded directly to the metal ion through covalent bonding [25]. A combination band at

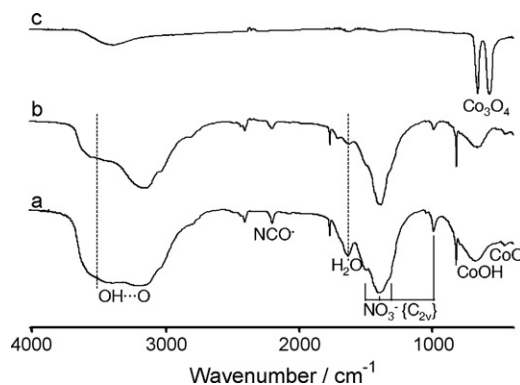


Fig. 3. Infrared spectra of the products evolved from the cobalt nitrate–urea mixture used as a catalyst precursor after heating at 343 (a), 413 (b), and 513 K (c).

2388 cm^{-1} was observed ($\nu_2 + \nu_3$) as well as narrow bands at 1763 and 825 cm^{-1} corresponding to intercalated, free nitrate ions in D_{3h} symmetry. In the low wavenumber region there were bands at 680 and 478 cm^{-1} due to the bending of Co–O–H and stretching of Co–O bonds, respectively. The infrared spectrum recorded for the sample heated at 413 K (Fig. 3b) was virtually identical to that obtained for the sample heated at 343 K, except for the partial disappearance of absorption bands at 1627 cm^{-1} and ca. 3500 cm^{-1} , according to water loss as suggested from TGA. The solid residue obtained after decomposition at 513 K was identified as the Co_3O_4 spinel. The infrared spectrum (Fig. 3c) showed two absorption bands, characteristic for cobaltites, at 578 and 664 cm^{-1} corresponding to the metal–oxygen stretching from octahedral and tetrahedral sites [26]. This was also supported by XRD (intense diffraction peaks at $d = 2.86, 2.44, 2.02, 1.56,$ and 1.43 \AA) and TPR (two hydrogen uptakes centered at 558 and 595 K corresponding to the reduction of Co_3O_4 into CoO and metallic Co, respectively).

The preparation route used for the in situ deposition of a cobalt oxide catalytic layer on ceramic, stainless-steel, and silicon walls was outstanding in terms of homogeneity and adherence. Fig. 4 shows SEM images corresponding to cobalt catalysts coatings over different substrates. In all cases, catalyst coatings were very homogeneous and well distributed. Fig. 4a corresponds to

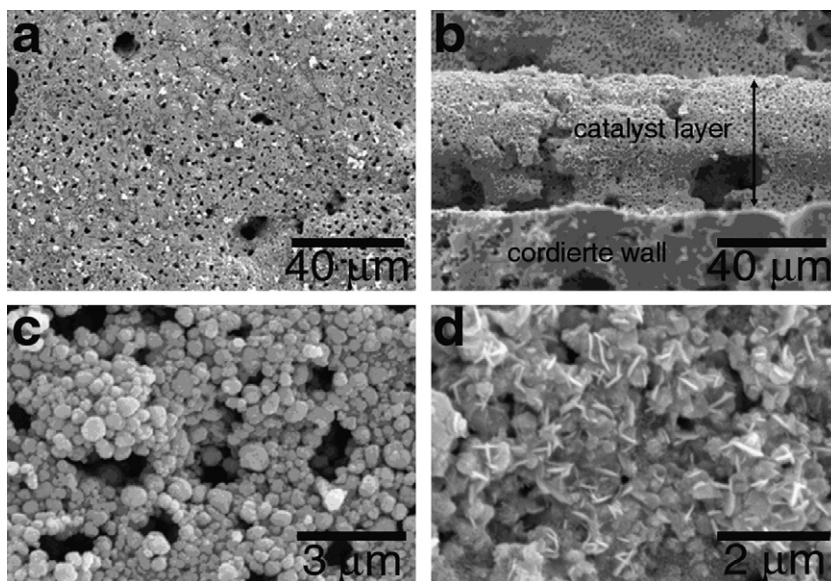


Fig. 4. Scanning electron microscopy images of catalyst coatings recorded at different magnification over ceramic monoliths (a–c) and stainless-steel (d) channels.

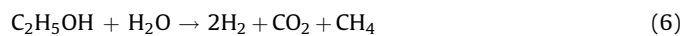
a representative image of the interior of a ceramic 400 cpsi channel. Pores of the cordierite substrate were still recognizable, meaning that the catalyst coating was thin. This is well exemplified by Fig. 4b, where the catalyst layer was imaged in profile view. A constant layer thickness of about 45–60 μm was measured in various channels and monoliths. As reported above, TGA indicated a high mass loss during preparation of catalyst coatings, which likely resulted in a volume reduction. In addition, the evolution of large amount of gases during the thermal decomposition (H_2O , NO_x , H_2CO , CO_2) helped to dissipate heat, thereby preventing sintering. Consequently, catalysts coatings were spongy and consisted entirely of spherical aggregates of about 0.2–0.6 μm in diameter (Fig. 4c). Similar homogeneous coatings were obtained over stainless-steel microchannels and silicon micromonoliths, although on these substrates the catalyst particle morphology at the micrometer scale changed from spherical to platelet-like (Fig. 4d). The adherence of catalysts coatings was checked by ultrasound exposure and by mechanical vibration. In all cases, a catalyst weight loss less than 2.5% occurred when the devices were subjected to 50 Hz and 10 G for 2 h. The catalyst weight loss monitored for ceramic monoliths after exposure to 40 kHz ultrasounds for 30 min was always between 2% (with ZnO binder) and 5%, whereas that of stainless-steel microchannels was about 20%. Stability experiments were not conducted over silicon micromonoliths due to the low catalyst loading (about 2 mg).

3.2. Ethanol steam reforming

3.2.1. Conventional monoliths

400 cpsi cordierite monoliths, catalytically coated as described above, were tested for ethanol steam reforming in slight/non-diluted conditions. No significant differences in catalytic behavior were observed between samples prepared with and without ZnO binder. Results from a series of seven experiments varying the feed concentration at constant temperature ($T = 673 \text{ K}$) and residence time (τ ca. 2.5 s) are presented in Fig. 5. Under the selected operating conditions, the hydrogen production (Q_{H_2}) in the monolithic reactor increased with the load (i.e., increase of the liquid feed, decrease of the inlet flow of N_2). Regarding the selectivities achieved for this series of experiences, Fig. 5 also includes the ratios of molar fractions between hydrogen and carbon dioxide ($y_{\text{H}_2}/y_{\text{CO}_2}$) and between carbon dioxide and carbon monoxide ($y_{\text{CO}_2}/y_{\text{CO}}$). The ratio $y_{\text{H}_2}/y_{\text{CO}_2}$ showed values of ca. 2.5 for non-diluted conditions; slightly lower than predicted by Eq. (1)

($y_{\text{H}_2}/y_{\text{CO}_2} = 3$). CO and methane concentrations also increased with the load ($y_{\text{CO}} \approx 7.6\%$, $y_{\text{CH}_4} = 14\%$), probably due to non-desired contribution of decomposition reactions under non-diluted conditions:



To compare the performance of the different reactors within this work, specific hydrogen production rates ($Q_{\text{H}_2}^2$ and $Q_{\text{H}_2}^3$) are used:

$$Q_{\text{H}_2}^2 = \frac{Q_{\text{H}_2} (\text{mL}_{\text{H}_2, \text{g}}/\text{min})}{Q_{\text{feed}, \text{l}} (\text{mL}_{\text{feed}, \text{l}}/\text{min}) \cdot V_{\text{reactor}} (\text{cm}^3_{\text{R}})} \quad (7)$$

$$Q_{\text{H}_2}^3 = \frac{Q_{\text{H}_2} (\text{mL}_{\text{H}_2, \text{g}}/\text{min})}{Q_{\text{feed}, \text{total}, \text{g}} (\text{mL}_{\text{feed}, \text{total}, \text{g}}/\text{min}) \cdot V_{\text{reactor}} (\text{cm}^3_{\text{R}})} \quad (8)$$

Defined by Eq. (7), $Q_{\text{H}_2}^2$ represents the hydrogen production rate per mL of liquid mixture fed and unit volume of the reactor. $Q_{\text{H}_2}^3$ (Eq. (8)) considers the total amount of gas fed to the reactor (to include the diluent). $Q_{\text{H}_2}^2$ presented a slight decrease with the load increase for conventional monoliths, with a maximum value achieved of $100 \text{ mL}_{\text{H}_2}/(\text{mL}_{\text{feed}, \text{l}} \text{ cm}^3_{\text{R}})$. Similarly to the absolute hydrogen production rate (Q_{H_2}) already presented in Fig. 5, $Q_{\text{H}_2}^3$ increased with the load (the residence time was the same for all experiences within this figure) up to a maximum of $0.077 \text{ mL}_{\text{H}_2}/(\text{mL}_{\text{feed}, \text{l}} \text{ cm}^3_{\text{R}})$. Despite higher values of $Q_{\text{H}_2}^2$ are achieved for the more diluted conditions, the operation of the reactor under practical conditions would be preferable under non-diluted scenarios, where higher molar fractions of hydrogen and higher absolute production rates can be attained.

3.2.2. Microreactor

Fig. 6 reports experimental results for ethanol steam reforming in the stainless-steel microreactor. Ethanol conversion (x_{EtOH}) of ca. 90% was achieved at 773 K under pure liquid feed. For this scenario, the reactor presented a very good performance, with measured values of $Q_{\text{H}_2}^2 = 2800 \text{ mL}_{\text{H}_2}/(\text{mL}_{\text{feed}, \text{l}} \text{ cm}^3_{\text{R}})$ and $Q_{\text{H}_2}^3 = 3 \text{ mL}_{\text{H}_2}/(\text{mL}_{\text{feed}, \text{total}, \text{g}} \text{ cm}^3_{\text{R}})$. Moreover, the microreactor showed values of specific H_2 -production rate ($Q_{\text{H}_2}^3$) four times higher than the cordierite monolith at the same temperature and feed dilution. An adequate $y_{\text{H}_2}/y_{\text{CO}_2}$ ratio of 3.3 and a good yield $\text{H}_2^{\text{produced}}/\text{EtOH}^{\text{fed}}$ of 4.1 were also measured for experiences

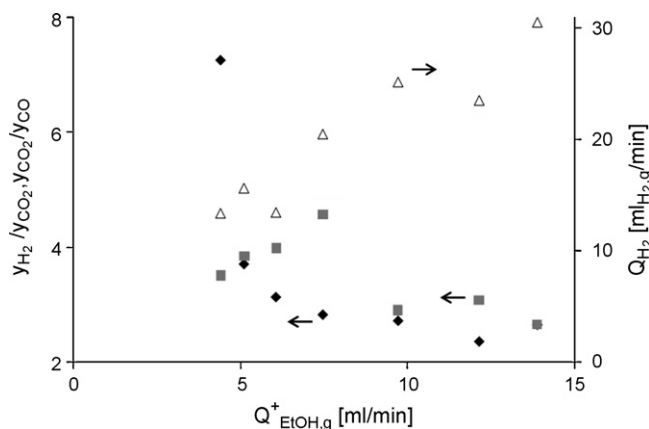


Fig. 5. Hydrogen production rate ($(\Delta) Q_{\text{H}_2}$) and outlet molar fraction ratios ($(\diamond) y_{\text{H}_2}/y_{\text{CO}_2}$ and $(\blacksquare) y_{\text{CO}_2}/y_{\text{CO}}$) for ethanol steam reforming over cordierite monoliths at different ethanol feeding flows ($Q_{\text{EtOH}, \text{g}}$). $T = 673 \text{ K}$, $\tau \sim 2.5 \text{ s}$, ethanol:water = 1:6 M (S/C = 3).

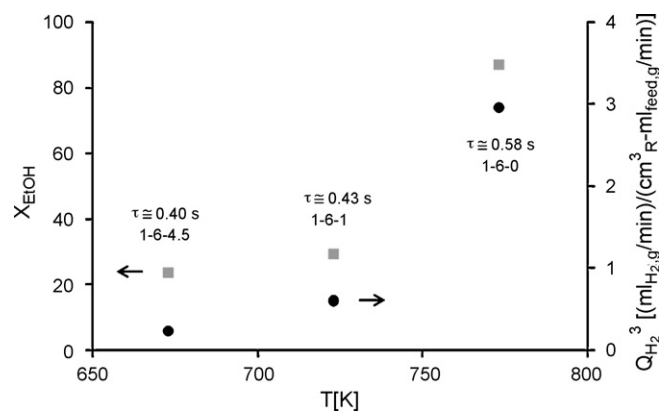


Fig. 6. Ethanol conversion ($(\blacksquare) x_{\text{EtOH}}$) and specific hydrogen production rate ($(\bullet) Q_{\text{H}_2}^3$) for ethanol steam reforming over the microreactor operating at different temperatures. Residence time (τ) and feed concentration (as ethanol:water: nitrogen molar ratios) are reported for each experience.

without N₂ in the feed. An achieved $y_{\text{CO}} \sim 4\%$ would suggest the utilization of a shift reactor of reduced dimensions after this reforming stage. Methane formation could be kept low in all microreactor experiments ($y_{\text{CH}_4} \sim 3\%$). As conclusion for the microreactor operation, non-diluted feed and temperatures of ca. 773 K are recommended. Despite some carbon formation was detected ($\sim 5 \times 10^{-3} \text{ g}_\text{C}/\text{g}_\text{cat} \text{ h}$), no significant deactivation was observed after about 30 h of operation (25 h without feeding N₂).

3.2.3. Silicon micromonolith

The above-described Si-micromonolithic reactor was also tested aiming at hydrogen production for micro-fuel cell operation via ethanol reforming. Outstanding results were achieved for this novel catalytic system, first reported in [8]. Fig. 7 shows the reactor performance at constant $T = 773 \text{ K}$ under different residence times (τ from 0.002 to 0.12 s) using a N₂ carrier flow (nitrogen inlet molar fraction, $y_{\text{N}_2} \sim 0.4$). Fig. 7a reports ethanol conversions and hydrogen production rates (both absolute and specific, Q_{H_2} and $Q_{\text{H}_2}^2$, respectively). Complementary, the corresponding selectivities to the gaseous products of the reaction (S_i , with $i = \text{H}_2, \text{CO}_2, \text{CO}$ and CH_4) are presented in Fig. 7b. A great variation of the feeding liquid flow was performed in this series of experiences; in fact, each point to the right in the x -axis of Fig. 7a comprises a reduction factor of 2 of the liquid flow fed (i.e., $\tau \sim$ doubles; factor 60 between edges). An ethanol conversion of ca. 4% was achieved for extremely low residence times of 2 ms. The highest value of x_{EtOH} ($\sim 43\%$) was achieved with a residence time of 0.12 s, for the selected operating conditions. As the liquid load decreased, the total amount of

Table 1

Si-micromonolithic reactor performance at different temperatures

T (K)	x_{EtOH}	S_{H_2}	S_{CH_4}	S_{CO}	S_{CO_2}	$Q_{\text{H}_2}^2$ ((mL _{H₂} /min)/(mL _{feed,1} /min) cm _R ³)
723	6.8	82.1	2.3	1.6	14.0	5,800
748	10.6	83.6	2.7	1.9	11.8	7,990
773	13.9	85.3	3.2	2.2	9.3	9,300
798	22.4	87.2	3.6	2.7	6.5	13,450
823	30.0	84.8	5.5	4.7	5.0	17,200

Ethanol conversion (x_{EtOH}), selectivities to the different gaseous products of reaction (S_i , with $i = \text{H}_2, \text{CO}_2, \text{CO}$ and CH_4) and specific H₂ production rate ($Q_{\text{H}_2}^2$) are reported. $\tau \sim 9 \times 10^{-3} \text{ s}$, feed composition: EtOH:H₂O:N₂ = 1:6:4.5 (molar).

hydrogen produced also decreased since it could not be compensated by the increase in ethanol conversion. Conversely, the quotient between these two quantities, defining the specific production rate ($Q_{\text{H}_2}^2$, see Eq. (7)), increased with the residence time up to spectacular values of $> 5 \times 10^4 \text{ mL}_{\text{H}_2}/(\text{mL}_{\text{feed,1}} \text{ cm}_R^3)$. Fig. 7b reports a change in the selectivity profile from an extremely low residence time/low conversion scenario to a low τ /medium x_{EtOH} one. For the first situation a high $y_{\text{H}_2}/y_{\text{CO}_2}$ ratio of 12, small amounts of CH₄, and no-measurable CO concentrations pointed out the prevalence of ethanol dehydrogenation and decomposition reactions. In contrast, for medium conversion scenarios, adequate selectivities were achieved leading to conveniently high hydrogen molar fractions and low CO outlet concentrations. The Si-micromonolithic reactor operation at different temperatures (from 723 to 823 K) was tested also under concentrated feed conditions (Table 1). An increase in temperature leads to an obvious increase in ethanol conversion and hydrogen production. Especially remarkable are the achieved values of $Q_{\text{H}_2}^2$, despite the up-to-medium-values in ethanol conversion. Also noticeable from Table 1, the CO₂ outlet molar fraction drops at increasing temperature, probably due to equilibrium limitations in the water-gas shift reaction. After ca. 80 h operation no deactivation was noticed. As stated above, tremendously high specific production rates of hydrogen can be achieved by this device. Its enormous contact area/reactor volume ratio is responsible of the ethanol conversions achieved despite the extremely low τ selected.

3.2.4. Comparison between catalytic devices

A direct comparison between the three catalytic wall reactors used in this work is not straightforward. Although the same

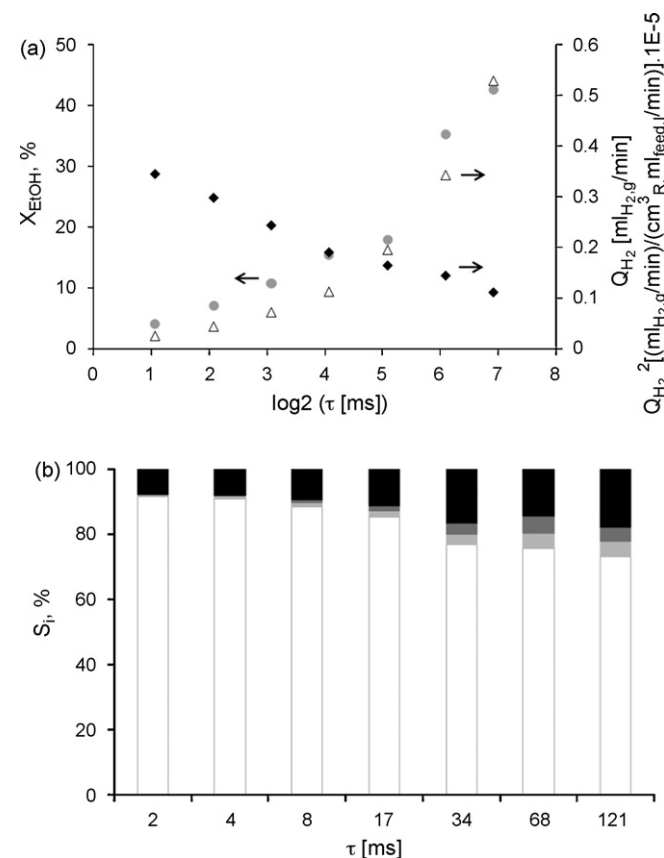


Fig. 7. Ethanol steam reforming over the Si-micromonolith under different residence times (τ). Ethanol conversion (\bullet) x_{EtOH} and both absolute and specific hydrogen production rates (\blacklozenge) Q_{H_2} and (\blacktriangle) $Q_{\text{H}_2}^2$ are shown in (a). (b) Reports the corresponding selectivities to the gaseous products of the reaction (S_i , with i : (\square) H₂, (\blacksquare) CO₂, (\square) CO and (\blacksquare) CH₄). $T = 773 \text{ K}$, ethanol:water:nitrogen = 1:6:4.5 M.

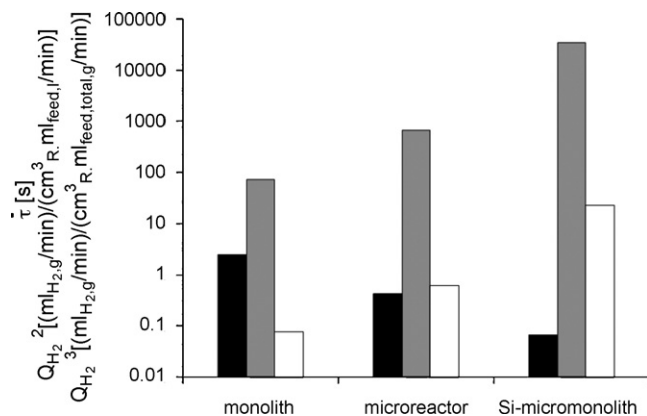


Fig. 8. Comparison of the performances of the three catalytic wall reactors used in this study in terms of specific H₂ production rates (\blacksquare) $Q_{\text{H}_2}^2$ and (\square) $Q_{\text{H}_2}^3$ and their corresponding residence time (\blacksquare) τ operating at a similar ethanol conversion level ($x_{\text{EtOH}} \sim 33\%$). Experimental conditions: monolith: $T = 673 \text{ K}$, EtOH:H₂O:N₂ = 1:6:0 M; microreactor: $T = 723 \text{ K}$, EtOH:H₂O:N₂ = 1:6:1 M; Si-micromonolith: $T = 773 \text{ K}$, EtOH:H₂O:N₂ = 1:6:4.5 M.

catalyst formulation was used, the different size of the units prevents the use of exactly the same operational conditions. Therefore, as mentioned above, the measurement of the reactor performance via specific measurements is used. Fig. 8 shows typical results regarding specific production of hydrogen ($Q_{\text{H}_2}^2$ and $Q_{\text{H}_2}^3$) for the three systems operating at similar ethanol conversion levels ($x_{\text{EtOH}} \sim 32\%$). Residence times in each situation are reported as well. Tremendous advantages in specific H_2 production can be achieved by miniaturizing the catalytic support. In fact, the outstanding increase achieved in the specific geometric surface (i.e., increase of the reaction rate per unit reactor volume; see Fig. 1) appears as the main responsible for the observed increase in reactor performance. An increase in specific H_2 production of about 1 order of magnitude is measured when passing from cordierite monolith to microreactor and of 1–2 orders of magnitude from microreactor to Si-micromonolith. The increase in both hydrogen specific production rates is also verified when compared on a catalyst mass basis instead of reactor volume (as calculated from data in Fig. 1). The selectivity distribution is nearly the same for both the microreactor and the micromonolith for the experiences under comparison in Fig. 8, whereas the hydrogen molar fraction achieved by the monolith is around 18% lower and the outlet CO molar fraction almost doubles when compared to the other systems. Also remarkable is the residence time distribution maintaining comparable conversion levels: from seconds for the monolithic reactor dropping to milliseconds for the Si-micromonolith. This capability emphatically suggests the study of this novel support to conduct reactions requiring low residence times; partial oxidation (PO) reactions for hydrogen production [27] being interesting candidates. Moreover, in PO reactions the high thermal conductivity and highly reproducible geometry of the substrate would be of great interest in favoring temperature control and avoiding local hot spots occurrence, respectively. The modular shape of the Si-micromonolith straightforwardly suggests increasing the ethanol conversion (and the H_2 production) by stacking several units in series. A compact unit housing several Si-micromonoliths is currently under manufacture.

4. Conclusions

The most studied catalytic wall systems are probably ceramic monoliths and foams. By decreasing the dimensions of their channels and the reaction volumes to the micrometer range, enhanced properties can be obtained. We have shown that the ethanol steam reforming reaction can be effectively performed at low temperature over cobalt catalysts in a wide range of channel dimensions, ranging from conventional monoliths (channel width of 0.9 mm) to semicylindrical microchannels (0.35 mm radius) and to silicon micromonoliths (channel diameter of 3–4 μm). Catalyst coatings were successfully prepared inside the channels from nitrate precursor and urea by an in situ route involving the formation of two-dimensional layered hydroxide salts, and showed a remarkable high homogeneity and mechanical stability. All three reforming

systems were tested under non-diluted/slightly diluted ethanol-water ($S/C = 3$) feed mixtures. Maximum ethanol conversions of ca. 70% and 90% ($\tau = 2.5$ and 0.5 s) were measured for monolith and microreactor operation, respectively. The Si-micromonolithic reactor proved extremely promising for hydrogen production for use in micro-fuel cell operation. Spectacular specific H_2 production rates of $> 52,000 \text{ mL}_{\text{H}_2} / (\text{mL}_{\text{feed},1} \text{ cm}_R^3)$ were measured for ca. 42% ethanol conversion and residence times in the order of milliseconds. The selectivity distribution was adequate, with high H_2 and low CO and CH_4 outlet molar fractions. No deactivation was observed after about 80 h of operation.

Acknowledgement

This work has been funded through MEC grant ENE2006-06925.

Appendix A. Supplementary data

Supplementary data associated with this article can be found, in the online version, at doi:10.1016/j.cattod.2008.08.040.

References

- [1] P.D. Vaidya, A.E. Rodrigues, Chem. Eng. J. 117 (2006) 39.
- [2] A. Haryanto, S. Fernando, N. Murali, S. Adhikari, Energy Fuels 19 (2005) 2098.
- [3] M. Ni, Y.C. Leung, M.K.H. Leung, Int. J. Hydrogen Energy 32 (2007) 3238.
- [4] R.M. Navarro, M.A. Peña, J.L.G. Fierro, Chem. Rev. 107 (2007) 3952.
- [5] D.R. Palo, R.A. Dagle, J.D. Holladay, Chem. Rev. 107 (2007) 3992.
- [6] Y. Men, G. Kolb, R. Zapf, V. Hessel, H. Löwe, Process Saf. Environ. Protect. 85 (2007) 413.
- [7] A. Casanovas, M. Saint-Gerons, F. Griffon, J. Llorca, Int. J. Hydrogen Energy 33 (2008) 1827.
- [8] J. Llorca, A. Casanovas, T. Trifonov, A. Rodríguez, A. Alcubilla, J. Catal. 255 (2008) 228.
- [9] J. Llorca, N. Homs, J. Sales, P. Ramírez de la Piscina, J. Catal. 209 (2002) 306.
- [10] J. Llorca, P. Ramírez de la Piscina, J.A. Dalmon, J. Sales, N. Homs, Appl. Catal. B 43 (2003) 355.
- [11] J. Llorca, N. Homs, J. Sales, J.L.G. Fierro, P. Ramírez de la Piscina, J. Catal. 323 (2004) 470.
- [12] J.A. Torres, J. Llorca, A. Casanovas, M. Domínguez, J. Salvadó, D. Montané, J. Power Sources 169 (2007) 158.
- [13] S. Freni, S. Cavallaro, N. Mondello, L. Spadaro, F. Frustreri, Catal. Commun. 4 (2003) 259.
- [14] J. Sun, X.-P. Qiu, F. Wu, W.-T. Zhu, Int. J. Hydrogen Energy 30 (2005) 437.
- [15] F. Mariño, G. Baronetti, M. Jobbagy, M. Laborde, Appl. Catal. A 238 (2003) 41.
- [16] M.S. Batista, R.K.S. Santos, E.M. Assaf, J.M. Assaf, E.A. Ticianelli, J. Power Sources 134 (2004) 27.
- [17] H. Song, L. Zhang, R.B. Watson, D. Braden, U.S. Ozkan, Catal. Today 129 (2007) 346.
- [18] H. Wang, J.L. Ye, Y. Liu, Y.D. Li, Y.N. Qin, Catal. Today 129 (2007) 305.
- [19] M. Benito, R. Padilla, L. Rodríguez, J.L. Sanz, L. Daza, J. Power Sources 169 (2007) 167.
- [20] A. Kaddouri, C. Mazzocchi, Catal. Commun. 5 (2004) 339.
- [21] F. Haga, T. Nakajima, H. Miya, S. Mishima, Catal. Lett. 48 (1997) 223.
- [22] G.G.C. Arizaga, K.G. Satyanarayana, F. Wypych, Solid State Ionics 178 (2007) 1143.
- [23] A. Loaiza-Gil, J. Arenas, M. Villarroel, F. Imbert, H. del Castillo, B. Fontal, J. Mol. Catal. A 228 (2005) 339.
- [24] T.N. Armes, M. Rajamathi, P.V. Kamath, Solid State Sci. 5 (2003) 751.
- [25] M. Rajamathi, P.V. Kamath, Int. J. Inorg. Mater. 3 (2001) 901.
- [26] O. Carp, L. Patron, A. Reller, J. Therm. Anal. Cal. 73 (2003) 867.
- [27] L.D. Schmidt, E.J. Klein, C.A. Leclerc, J.J. Krummenacher, K.N. West, Chem. Eng. Sci. 58 (2003) 1037.